

SCIENTIFIC REPORTS



OPEN

Imaging of current density distributions with a Nb weak-link scanning nano-SQUID microscope

Yusuke Shibata¹, Shintaro Nomura¹, Hiromi Kashiwaya², Satoshi Kashiwaya², Ryosuke Ishiguro^{3,4} & Hideaki Takayanagi⁴

Received: 18 June 2015

Accepted: 15 September 2015

Published: 13 October 2015

Superconducting quantum interference devices (SQUIDs) are accepted as one of the highest magnetic field sensitive probes. There are increasing demands to image local magnetic fields to explore spin properties and current density distributions in a two-dimensional layer of semiconductors or superconductors. Nano-SQUIDs have recently attracting much interest for high spatial resolution measurements in nanometer-scale samples. Whereas weak-link Dayem Josephson junction nano-SQUIDs are suitable to miniaturization, hysteresis in current-voltage (*I-V*) characteristics that is often observed in Dayem Josephson junction is not desirable for a scanning microscope. Here we report on our development of a weak-link nano-SQUIDs scanning microscope with small hysteresis in *I-V* curve and on reconstructions of two-dimensional current density vector in two-dimensional electron gas from measured magnetic field.

Superconducting quantum interference devices (SQUIDs) utilize phase difference of two-weakly coupled superconducting electrodes with Josephson junctions or weak links forming a superconducting loop¹. The supercurrent flowing in a SQUID is a periodical function of the flux penetrating the superconducting loop Φ divided by the magnetic flux quantum $\Phi_0 = h/2e = 2.0679 \times 10^{-15}$ Wb. SQUIDs have been widely used as one of the most sensitive magnetic sensors²⁻⁶. Images of magnetic flux are captured by a SQUID probe scanned on the surface of a sample^{2,4}. Since there has been increasing interests in detecting magnetic field of small area in order to characterize nanostructures or nano-devices, nano-meter scale SQUIDs have been actively studied recently. Decreasing the size of the superconducting loop favours sensitivity to local magnetic dipoles due to decrease in the limiting flux spectral density³ and due to reduced distance between magnetic dipoles and the SQUID loop^{7,8}. The size of the superconducting loop was typically 2–100 μm ^{2,4,9}. Recently, a self-aligned SQUID has been fabricated on a tip of a sharpened quartz tube in the range of 40–300 nm in diameter and has been used for scanning probe magnetometry⁶. This method has the highest spatial resolution to date, but the high flexibility of the design and configuration of SQUIDs makes weak-link nano-SQUIDs fabricated by a focused ion beam (FIB) process^{10,11} attractive for use as local probe of magnetic flux.

Weak-link superconducting junctions are fabricated by direct milling using Ga⁺ ions without lithography process. Simultaneous observations of milled area enable us to precisely position the SQUID and control the properties of the weak-link superconducting junctions^{10,11}. This is especially advantageous to fabricate a weak-link nano-SQUID on a tip of a scanning probe. Multiple SQUIDs may be fabricated on a scanning probe by FIB process, which may find applications for mappings of magnetic field vector. Weak-link SQUIDs have a number of advantages over tunnel junction based SQUIDs. Since the size of

¹Division of Physics, University of Tsukuba, Tennodai, Tsukuba, 305-8571, Japan. ²National Institute of Advanced Industrial Science and Technology (AIST), Umezono, Tsukuba, 305-8568, Japan. ³Department of Mathematical and Physical Sciences, Faculty of Science, Japan Women's University, Mejirodai, Bunkyo-ku, Tokyo 112-8681, Japan.

⁴Department of Applied Physics, Faculty of Science, Tokyo University of Science, Niijuku, Katsushika-ku, Tokyo 125-8585, Japan. Correspondence and requests for materials should be addressed to S.N. (email: nomura.shintaro.ge@u.tsukuba.ac.jp)

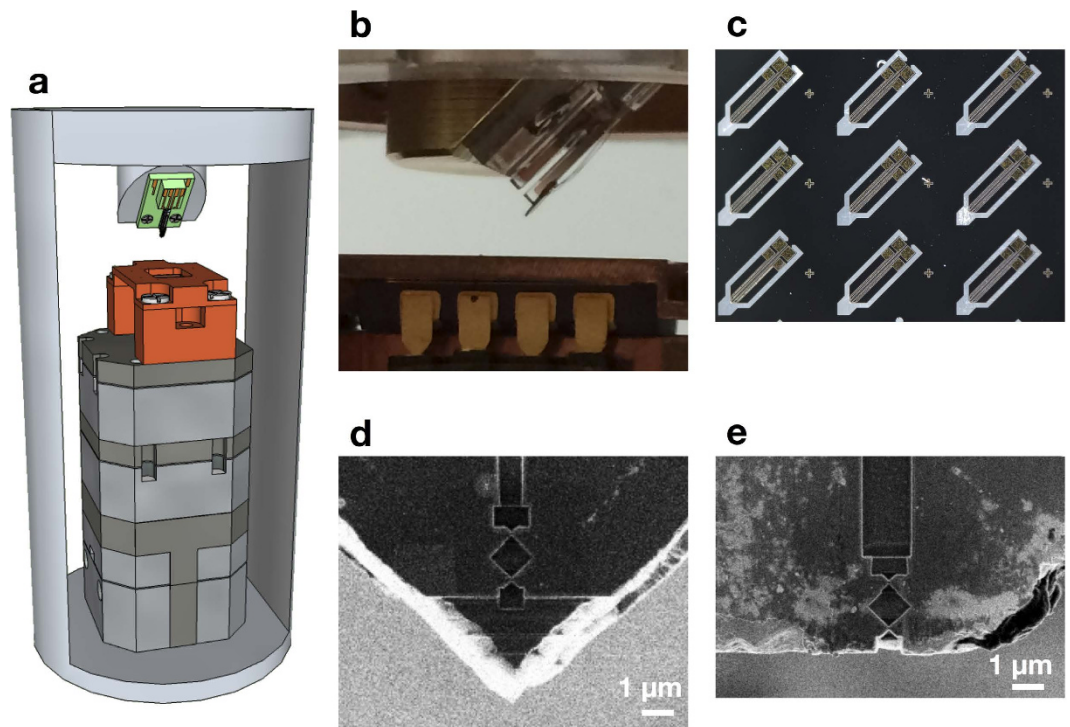


Figure 1. Schematics of scanning nano-SQUID system and images of nano-SQUID probes. (a) Schematic illustration of a scanning nano-SQUID system in a cryogen-free ^4He refrigerator. Upper green part indicates a holder for a scanning SQUID probe attached to a quartz tuning fork. A sample stage is placed on triaxial piezoelectric inertial stages. The SQUID probe and the piezoelectric inertial stages are settled in a stainless housing which is connected to the 4K plate with four springs. (b) Optical image of a SQUID probe attached to a tuning fork and a sample chip carrier. (c) Optical image of probes fabricated by a laser-lithography and deep etching of a silicon substrate. After detaching each pieces, a nano-SQUID was fabricated at the tip of the probe by an FIB. (d) Scanning ion microscope images of SQUID probes without mechanical polishing and (e) after mechanical polishing of the tip of the probe. SQUID loop and weak link junctions were fabricated by an FIB milling system.

weak-link junctions can typically be made smaller than the size of tunnel junction, the capacitance and the inductance are smaller in weak-link junctions than those in tunnel junction based SQUIDs. This increases sensitivity to magnetic flux and tolerance for high magnetic field environments. However, the presence of hysteresis in current-voltage (I - V) characteristics¹⁰ has been an obstruct for a weak-link nano-SQUID to be used in scanning probe measurements.

In this paper, we describe construction and characterization of our weak-link scanning nano-SQUID microscope (Fig. 1(a–e)) with small hysteresis in I - V characteristics suitable for imaging. We present results of imaging of magnetic field created by current in a Hall-bar structure of a GaAs/ $\text{Al}_{0.3}\text{Ga}_{0.7}\text{As}$ modulation-doped single heterojunction to evaluate performance of the weak-link scanning nano-SQUID microscope, and report on reconstruction of the two-dimensional current density vector by a Fourier analysis.

Fabrication of weak-link nano-SQUID probes

Nb/Au thin films were deposited on a Si substrate. Nb film with the thickness of 23 nm was deposited by an RF-sputtering and subsequently Au film with the thickness of 70 nm was deposited by an electron-beam deposition at the base pressure of 6×10^6 Pa. The Au thin film was used to protect the Nb film from Ga^+ ion beam exposure. The Au thin film was also important to reduce the hysteresis in the I - V curve of a nano-SQUID by reducing the self-heating effect at the weak-link junctions^{10,12}. Superconducting four-terminal configurations were patterned by a maskless laser lithography using 405 nm light (DL-1000, NanoSystem Solution, inc). Silicon probes for scanning microscopy with a thickness of 100 μm and the size of $2000 \times 600 \mu\text{m}^2$ were defined by a maskless laser lithography. Deep etching of silicon substrate with high aspect ratio was performed by 200 cycles of a pulsed reactive ion etching (RIE) by SF_6 and deposition of a C_4F_8 passivation layer. About a hundred pieces of Si probes were fabricated by the above process. (Fig. 1(c)) The tip of a part of Si probes was mechanically polished (Supplementary Fig. 1, and Supplementary Note 1) to remove Nb/Au film near the edge damaged by the RIE process using Al_2O_3 powder with an average diameter of 100 nm dispersed in 1-octanol. Each Si

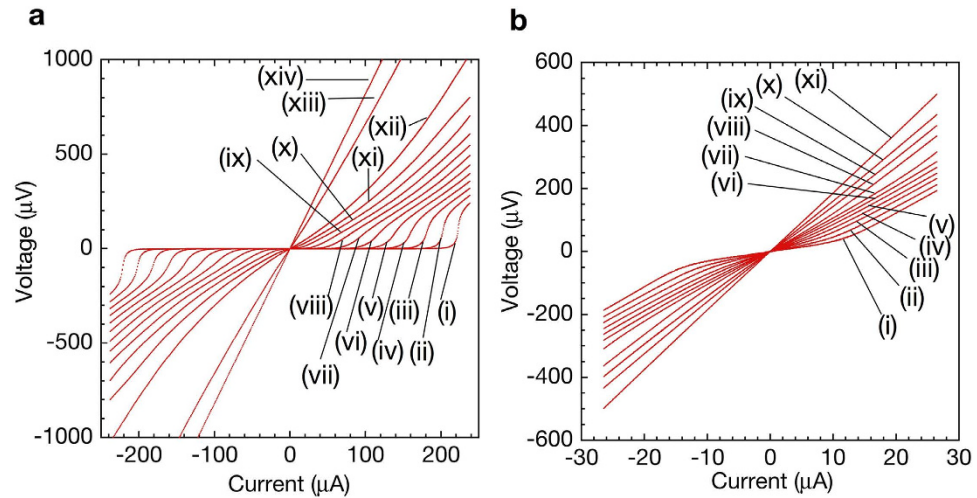


Figure 2. Temperature dependence of current-voltage characteristics of SQUID probes. (a) Current-voltage characteristics of a SQUID probe without mechanical polishing at $T =$ (i) 3.6, (ii) 3.8, (iii) 4.0, (iv) 4.2, (v) 5.0, (vi) 5.2, (vii) 5.4, (viii) 5.6, (ix) 5.8, (x) 6.0, (xi) 6.2, (xii) 6.4, (xiii) 6.6, (xiv) 6.8 K. The current was swept for both negative and positive directions, and no hysteresis in the I - V characteristics was observed. (b) Current-voltage characteristics of a SQUID probe after mechanical polishing at $T =$ (i) 3.6, (ii) 3.8, (iii) 4.0, (iv) 4.2, (v) 5.0, (vi) 5.2, (vii) 5.4, (viii) 5.6, (ix) 5.8, (x) 6.0, (xi) 6.2 K. No hysteresis in the I - V characteristics was observed.

probe was cut into a piece. A Si probe was mounted on a quartz tuning fork with a resonance frequency of 32,768 Hz. After gluing the Si probe to a quartz tuning fork, the resonance frequency decreases to typically 30.8 KHz with the Q-factor of about 10,000 at 4 K. Finally, the superconducting loop and weak-link junctions were milled by the FIB process with typical beam voltage and current of 31 kV and 5 pA, respectively. The SQUID loop with the size of $1 \mu\text{m}$ was located within $4.8 \mu\text{m}$ from the tip of the Si probe. The dimensions of the SQUID loop and the weak-link width were $1.0 \mu\text{m}$ and 80 nm , respectively. (Fig. 1(d,e)) The geometrical inductance $L = 5\mu_0 C/16$, where C is the inner circumference of the SQUID¹³ was 1.6 pH . The effect of the self-induced field as given by $\beta = 2LI_c/\Phi_0$ was 0.32 .

Results and Discussion

Characteristics of SQUID probes. Figure 2(a,b) show I - V characteristics of nano-SQUID probes without and after mechanical polishing, respectively, at temperatures between $T = 3.6$ and 6.8 K at zero applied magnetic field. The current was swept in both negative and positive directions, and no hysteresis was observed in the I - V characteristics in Fig. 2(a,b). The Dayem nano-SQUID was shown to exhibit a hysteretic behaviour for $L_{\text{SQ}}/\xi > 3.5^{14}$, where L_{SQ} is the Dayem nano bridge size and ξ is the Ginzburg-Landau coherence length, which is 38 nm for Nb¹. The constrictions of the nano-SQUID were milled to wedged shape by the FIB process with the weak link width of $w = 80 \text{ nm}$. Although the model by Likharev¹⁴ is not directly applicable to the geometry of our nano-SQUIDs, the nonhysteretic behaviour of I - V characteristics is explained by small $w/\xi = 2.1$. Furthermore, we reduced the effects of Joule heating by reducing the critical current I_c and preparing Au film above Nb film for heat conduction, which is also important for the nonhysteretic behaviour of I - V characteristics of our nano-SQUIDs.

The critical temperature T_c of the nano-SQUID without mechanical polishing was 6.0 K , which is reduced from typical T_c of Nb of 9.2 K due to small thickness of the Nb film and the proximity effect between Nb and Au¹⁰. Figure 3(a) shows a typical I - V characteristics of the nano-SQUID probe without mechanical polishing (Fig. 1(d)) at applied magnetic fields between 0.1 and 0.5 mT at 4.2 K . The critical current I_c is seen to change with the applied magnetic field.

The SQUID loop of the probe after mechanical polishing of the tip of the nano-SQUID probe (Fig. 1(e)) was located very close to the edge of the Si substrate and the probe did not exhibit zero resistance as shown in Fig. 2(b) above 3.6 K because of the damage of Nb film during the fabrication process. Nevertheless, the change of the voltage with the applied magnetic field was observed as shown in Fig. 3(b), indicating that this nano-SQUID probe is useful as a magnetic field sensor. The nonhysteretic behaviour of our nano-SQUIDs enables us to measure the voltage of a nano-SQUID at a constant bias current to obtain magnetic flux threading the SQUID loop. This is particularly advantageous to use a nano-SQUID as a magnetic sensor for a scanning microscope. If a nano-SQUID shows a hysteretic I - V characteristic, I_c has to be measured by sweeping I at each point. Typical voltage-magnetic field ($V_{\text{SQ}} - B_{\text{ext}}$) characteristics in Fig. 3(c,d) show oscillations of SQUID voltage V_{SQ} with B_{ext} at constant current-bias. The noise of the probe without mechanical polishing was estimated to be $3.1 \text{ nT}/\sqrt{\text{Hz}}$ at 2 kHz . The noise

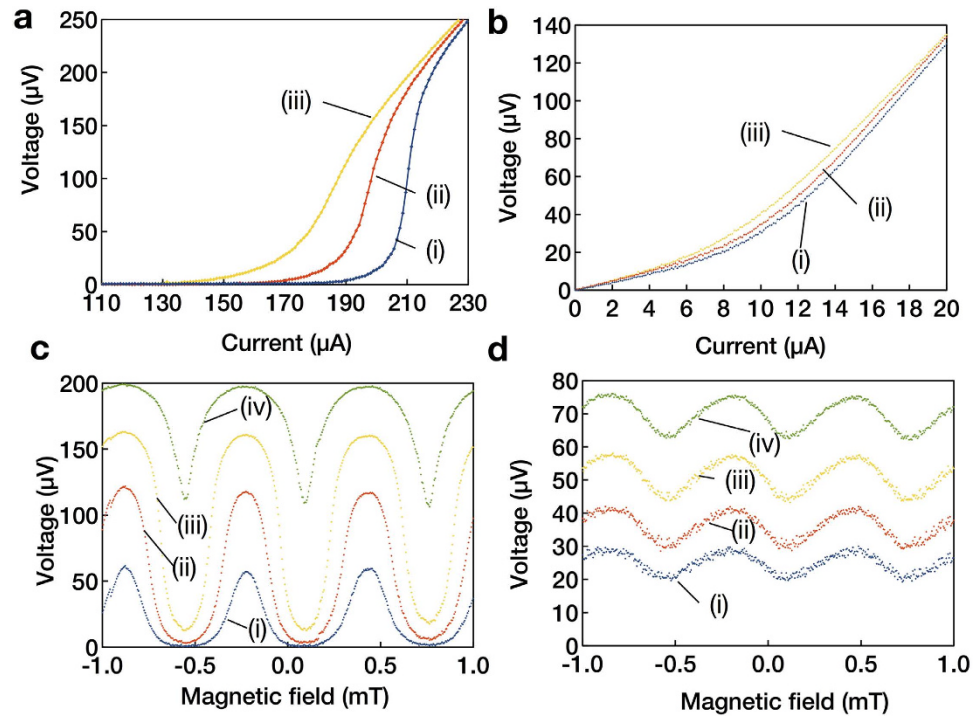


Figure 3. Magnetic field dependence of current-voltage characteristics of SQUID probes and modulation of the SQUID voltage by magnetic field. (a) Typical current-voltage characteristics of a nano-SQUID probe without mechanical polishing and (b) after mechanical polishing of the tip of the probe at applied magnetic field of (i) 0.5, (ii) 0.3, and (iii) 0.1 mT. No hysteresis in the I - V characteristics was observed. (c) Modulation of SQUID voltage (V_{SQ}) by B_{ext} at current-bias of (i) 196.2, (ii) 198.1, (iii) 200.0, and (vi) 201.9 μA for a nano-SQUID probe without mechanical polishing. (d) Modulation of SQUID Voltage (V_{SQ}) in B_{ext} at current-bias of (i) 8.0, (ii) 10.0, (iii) 12.0, and (vi) 14.0 μA for a nano-SQUID probe after mechanical polishing.

of the probe after mechanical polishing was degraded to $40 \text{ nT}/\sqrt{\text{Hz}}$ at 2 kHz while the spatial resolution was improved.

Mapping of magnetic field distribution around Nb/Au strips. Mapping of magnetic field distribution around Nb/Au strips was performed to test spatial resolution of our nano-SQUID microscope. The thicknesses of Nb and Au films were 600 and 30 nm, respectively. The width and the spacing of Nb/Au strips were 2 and 5 μm , respectively, as shown in Fig. 4(a). A nano-SQUID probe after mechanical polishing was used at a constant distance between the tip of the SQUID probe and the sample surface of 1.2 μm . The obtained mapping of magnetic field distribution of Nb/Au strips at an applied magnetic field of 1.05 mT is shown in Fig. 4(b). A strip of reduced magnetic field because of the Meissner effect of the Nb strips can be identified at $5 < x < 7 \mu\text{m}$. The reduction of magnetic field is more clearly seen in the lineprofiles of magnetic field along $y = 10, 15, \text{ and } 20 \mu\text{m}$ as shown in Fig. 4(c), indicating that the spatial resolution of our nano-SQUID microscope is better than 2 μm .

Mappings of magnetic field distribution induced by current in a modulation-doped single heterojunction sample. Results of mappings of magnetic field created by ac current between the voltage probes 1 and 2 of the Hall-bar structure (Fig. 5(a,b)) at $I_{\text{sample}} = 70$ and 2.8 μA are shown in Fig. 5(c,d), respectively, at $T = 4 \text{ K}$ at the applied magnetic field by a superconducting magnet of 0.0 mT using a probe after mechanical polishing. The measurements were performed in unshielded laboratory environment, and hence the sample and the nano-SQUID probe were subject to the environmental magnetic field. The size of the scanning area was $80 \times 80 \mu\text{m}^2$ with a step size of 2 μm for x - and y -directions. The height of the SQUID probe from the sample surface was $z_0 = 1.5 \mu\text{m}$. The voltage of a SQUID at a constant current bias of 12 μA changes due to magnetic field created by the current in the Hall-bar structure. This voltage change was synchronously detected with a lock-in amplifier at a time constant of 1 s by scanning the position of the nano-SQUID probe on the surface of the sample. The bias current of $I_{\text{sample}} = 70$ and 2.8 μA corresponds to current density of 7.0 and 0.28 A/m, respectively. The mapping in Fig. 5(c) (Fig. 5(d)) corresponds to the case of the current density above (below) the condition for the breakdown of the quantum Hall effect^{15,16}. The maximum source-drain voltage (V_{SD}) was

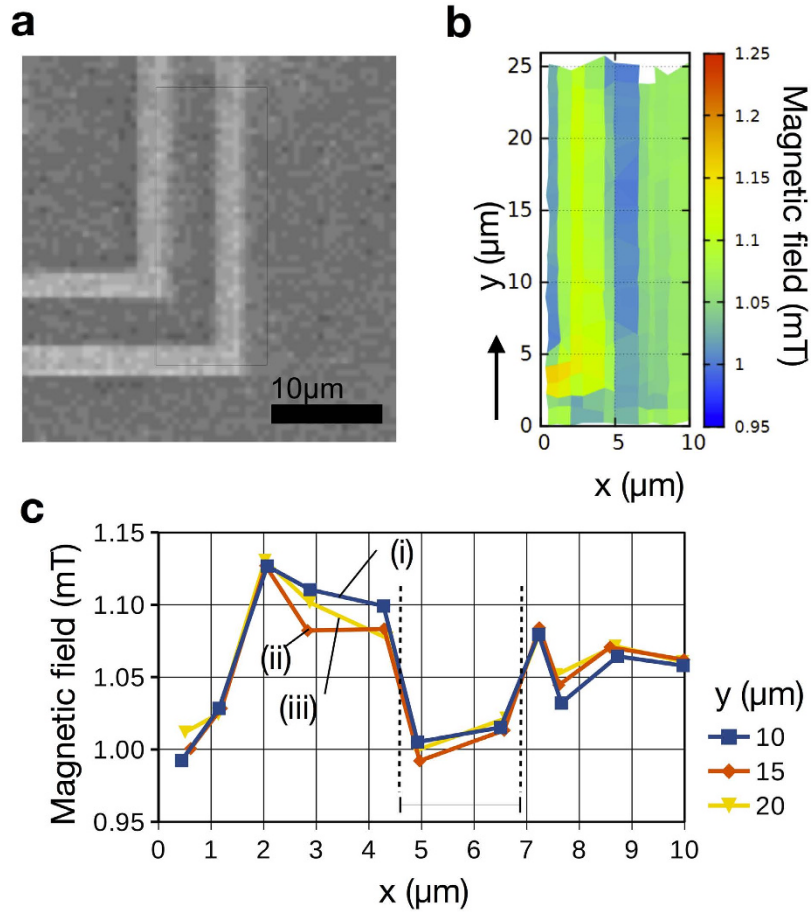


Figure 4. Image and mapping of magnetic field distribution of Nb/Au strips. (a) Scanning electron microscope image of Nb/Au strips with a width of $2\ \mu\text{m}$ and a spacing of $5\ \mu\text{m}$ at applied magnetic field of $1.05\ \text{mT}$ at $4\ \text{K}$. (b) Mapping of magnetic field distribution of Nb/Au strips. (c) Line profiles of magnetic field distribution along (i) $y = 10$, (ii) 15 , and (iii) $20\ \mu\text{m}$.

$8.0\ \text{mV}$ at $I_{\text{sample}} = 70\ \mu\text{A}$. The Fermi energy of the electrons is $\varepsilon_F = 12\ \text{meV}$ at the electron density of the sample of $n_s = 3.3 \times 10^{15}\ \text{m}^{-2}$, which gives $eV_{\text{SD}} < \varepsilon_F$. The positive and negative magnetic fields are observed near the edges of the stem of the Hall-bar structure with the width of $10\ \mu\text{m}$ as shown in Fig. 5(c). The magnetic field distributions are seen to be broadened in the center region where the $10\ \mu\text{m}$ width stem crosses with the bar with the width of $25\ \mu\text{m}$. Similar structures are seen in the magnetic field distribution at $I_{\text{sample}} = 2.8\ \mu\text{A}$ (Fig. 5(d)) although the signal-to-noise ratio was degraded.

Reconstruction of two-dimensional current density distribution. Two-dimensional current density distribution $\mathbf{J}(x, y)$ can be reconstructed from the measured magnetic flux distribution $\mathbf{B}(x, y, z)$ based on a Fourier analysis¹⁷. The two-dimensional Fourier transform of the current density and magnetic field is defined by

$$j_y(k_x, k_y) = \int_{-\infty}^{\infty} \int_{-\infty}^{\infty} J_y(x, y) e^{i(k_x x + k_y y)} dx dy \tag{1}$$

and

$$b_x(k_x, k_y, z) = \int_{-\infty}^{\infty} \int_{-\infty}^{\infty} B_x(x, y, z) e^{i(k_x x + k_y y)} dx dy, \tag{2}$$

respectively. By using the two-dimensional Fourier transform of the Green's function

$$g(k_x, k_y, z) = \frac{\mu_0 d}{2} e^{-k_0 z}, \tag{3}$$

we have

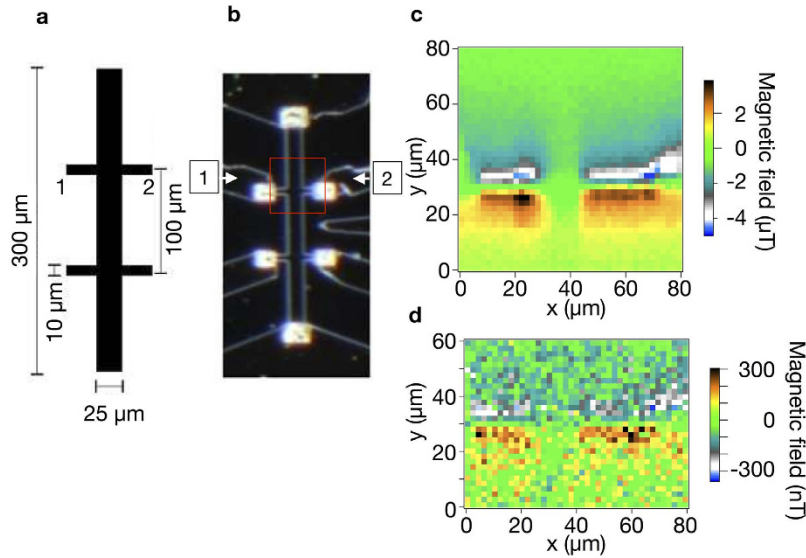


Figure 5. Hall-bar structure and mappings of magnetic field distribution by the current flowing in the Hall-bar sample. (a) Schematic structure of a sample Hall-bar. (b) Optical micrograph of a sample Hall-bar structure. Red square indicates the scanning area of $80\ \mu\text{m} \times 80\ \mu\text{m}$ for (c). Mappings of magnetic field distribution induced by current in a GaAs/Al_xGa_{1-x}As modulation-doped single heterojunction sample at $T = 4\ \text{K}$ for current (c) $I_{\text{sample}} = 70$ and (d) $2.8\ \mu\text{A}$ at the applied magnetic field by a superconducting magnet of $0.0\ \text{mT}$ using a nano-SQUID probe after mechanical polishing of the tip of the probe. The height of the SQUID probe from the sample surface was $1.5\ \mu\text{m}$.

$$b_x(k_x, k_y, z) = g(k_x, k_y, z)j_y(k_x, k_y), \quad (4)$$

where d is the thickness of the current and we defined $k_0 = \sqrt{k_x^2 + k_y^2}$. Similarly, b_z is given by

$$b_z(k_x, k_y, z) = ig(k_x, k_y, z) \left(\frac{k_y}{k_0} j_x(k_x, k_y) - \frac{k_x}{k_0} j_y(k_x, k_y) \right). \quad (5)$$

We assume quasi-stationary current density $\nabla \cdot \mathbf{J}(x, y) = 0$ in real-space and $-ik_x j_x(k_x, k_y) - ik_y j_y(k_x, k_y) = 0$ in k -space. A nano-SQUID probe facing θ to the surface of the sample detects $B_M(x, y, z) = B_x(x, y, z) \sin \theta + B_z(x, y, z) \cos \theta$. Because a nano-SQUID detects magnetic field averaged over the square SQUID loop, the Fourier transform of measured magnetic field $b_M(k_x, k_y, z)$ should be divided by¹⁷

$$h(k_x, k_y) = \frac{\sin(k_x L_{\text{SQ}}/2)}{k_x L_{\text{SQ}}/2} \frac{\sin(k_y L_{\text{SQ}}/2)}{k_y L_{\text{SQ}}/2}, \quad (6)$$

where L_{SQ} is the size of the SQUID loop to take into account the finite size of the SQUID in x - and y -directions. In the case of our nano-SQUID, $h(k_x, k_y)$ does not introduce noticeable difference because L_{SQ} is smaller than the step size of the measurement. For the z -direction, we assume a SQUID probe detects the average magnetic field B_{ave} at the effective height z_{eff} satisfying

$$B_{\text{ave}} = \frac{\mu_0 I}{2\pi} \frac{1}{L_{\text{SQ}} \sin \theta} \int_{z_0}^{z_0 + L_{\text{SQ}}} \frac{\sin \theta}{z} dz = \frac{\mu_0 I}{2\pi} \frac{1}{z_{\text{eff}}}. \quad (7)$$

For $z_0 = 1.5\ \mu\text{m}$, $L_{\text{SQ}} = 1.0\ \mu\text{m}$, and $\theta = 51^\circ$, we obtain $z_{\text{eff}} = 1.9\ \mu\text{m}$.

We substitute $j_x = -\frac{k_y}{k_x} j_y$, into equation (5), and using equation (4), we obtain

$$b_M(k_x, k_y, z_{\text{eff}}) = g(k_x, k_y, z_{\text{eff}}) (\sin \theta - i \frac{k_0}{k_x} \cos \theta) j_y(k_x, k_y). \quad (8)$$

The current density can be readily obtained as

$$j_y(k_x, k_y) = \frac{2}{g(k_x, k_y, z_{\text{eff}})} \frac{\sin \theta + i \frac{k_0}{k_x} \cos \theta}{\sin^2 \theta + \frac{k_0^2}{k_x^2} \cos^2 \theta} b_M(k_x, k_y, z_{\text{eff}}) \quad (9)$$

in k -space and

$$J_y(x, y) = \frac{1}{(2\pi)^2} \int_{-\infty}^{\infty} \int_{-\infty}^{\infty} j_y(k_x, k_y) e^{-i(k_x x + k_y y)} dk_x dk_y \quad (10)$$

in real-space. $J_x(x, y)$ may be similarly obtained by using $j_x = -\frac{k_y}{k_x} j_y$. For the case of $k_x = k_y = 0$, $j_x(0, 0)$ and $j_y(0, 0)$ cannot be determined from $b_M(k_x, k_y, z_{\text{eff}})$. The obtained J_x and J_y have ambiguity by uniform current density distribution. In the following analysis, we set this uniform current density as zero.

Figure 6(a–d) show reconstructed current density distributions $J_x(x, y)$ and $J_y(x, y)$ from the measured magnetic flux in Fig. 3(b,c) at $I_{\text{sample}} = 70$ and $2.8 \mu\text{A}$, respectively, for $\theta = 51^\circ$. Calculations were performed on a mesh of 128×128 in the x and y directions. A Parzen window^{17,18}

$$W(k) = \begin{cases} 1 - k/k_{\text{max}}, & k < k_{\text{max}} \\ 0, & k > k_{\text{max}} \end{cases} \quad (11)$$

was used to eliminate high-spatial-frequency components of measured mappings¹⁷. We empirically chose $k_{\text{max}} = 1.5 \times 10^6$ and $6.9 \times 10^5 \text{ m}^{-1}$ for $I_{\text{sample}} = 70$ and $2.8 \mu\text{A}$, respectively, so that high-spatial-frequency noise is effectively reduced with minimum loss of spatial resolution. In the center region, where the $10 \mu\text{m}$ -stem crosses the bar with the width of $25 \mu\text{m}$, the current density $J_x(x, y)$ is seen to spread to the wider bar. This can be more clearly indicated in $J_y(x, y)$ in Fig. 6(b) by the positive and negative current density near the corners of the mesa structure of the Hall-bar. At smaller current of $I_{\text{sample}} = 2.8 \mu\text{A}$, the main features of the current densities can still be resolved as shown in Fig. 6(c,d). Although the signal-to-noise ratio of the mapping of magnetic field in Fig. 5(d) is heavily degraded as compared to the case of $I_{\text{sample}} = 70 \mu\text{A}$ in Fig. 5(c), the current densities are recovered at the expense of degraded spatial resolution by using $k_{\text{max}} = 6.8 \times 10^5 \text{ m}^{-1}$ used for the Parzen window. The mappings of the magnetic field (Fig. 5(c)) and the reconstructed current density distributions (Fig. 6(a,b)) using the nano-SQUID probe after mechanical polishing show remarkably better spatial resolution as compared to the mappings using the nano-SQUID probe without mechanical polishing (Supplementary Fig. 2). This shows the advantage of the nano-SQUID probe after mechanical polishing over the unpolished nano-SQUID probe although the zero resistance was not observed due to the damage of Nb film in the polished nano-SQUID probe. The current obtained by integrating current densities $J_x(x, y)$ on the white bars in Fig. 6(a) is 84 and $91 \mu\text{A}$ for the crosssection A-B and C-D, respectively, in reasonable agreement with $I_{\text{sample}} = 70 \mu\text{A}$. Similarly, current across the white bars in Fig. 6(c) is 4.5 and $4.6 \mu\text{A}$ for the crosssection A-B and C-D, respectively, for $I_{\text{sample}} = 2.8 \mu\text{A}$.

Comparison of the measured current density with results of a numerical calculation.

Two-dimensional quasi-stationary current density is calculated by assuming that the current density instantaneously responds to the electric field at the position of the electron as given by¹⁹

$$\mathbf{J}(x, y) = -\sigma(x, y) \nabla \phi(x, y), \quad (12)$$

which is applicable to a low mobility limiting case. Clearly, this model is not directly applicable to high mobility electron gas, nonetheless this model is useful to assist the understandings of the observed current density mappings by our SQUID microscope. One may refer to semiclassical^{20,21} or quantum mechanical²² ballistic electron transport theories for more realistic descriptions. The measured current density $\mathbf{J}(x, y)$ may be described by the statistical or quantum mechanical average of the local electric current operator, which is described by the momentum \mathbf{p} and the position \mathbf{x} of an electron. Then ballistic electron transport theories take into account the scatterings of the electron from \mathbf{p} to \mathbf{p}' by such as the external electric field, the impurities, and the phonons. The description implied by equation (12) ignores these effects, in particular, the inertial motion of the current carrying electrons.

We also assume slow modulation frequency of the current with negligible displacement current $|\varepsilon \partial \mathbf{E} / \partial t| \ll |\mathbf{J}|$ and isotropic conductivity $\sigma(x, y) = \sigma_{xx}(x, y) = \sigma_{yy}(x, y)$. Then we solve numerically

$$\nabla \cdot (\sigma(x, y) \nabla \phi(x, y)) = 0 \quad (13)$$

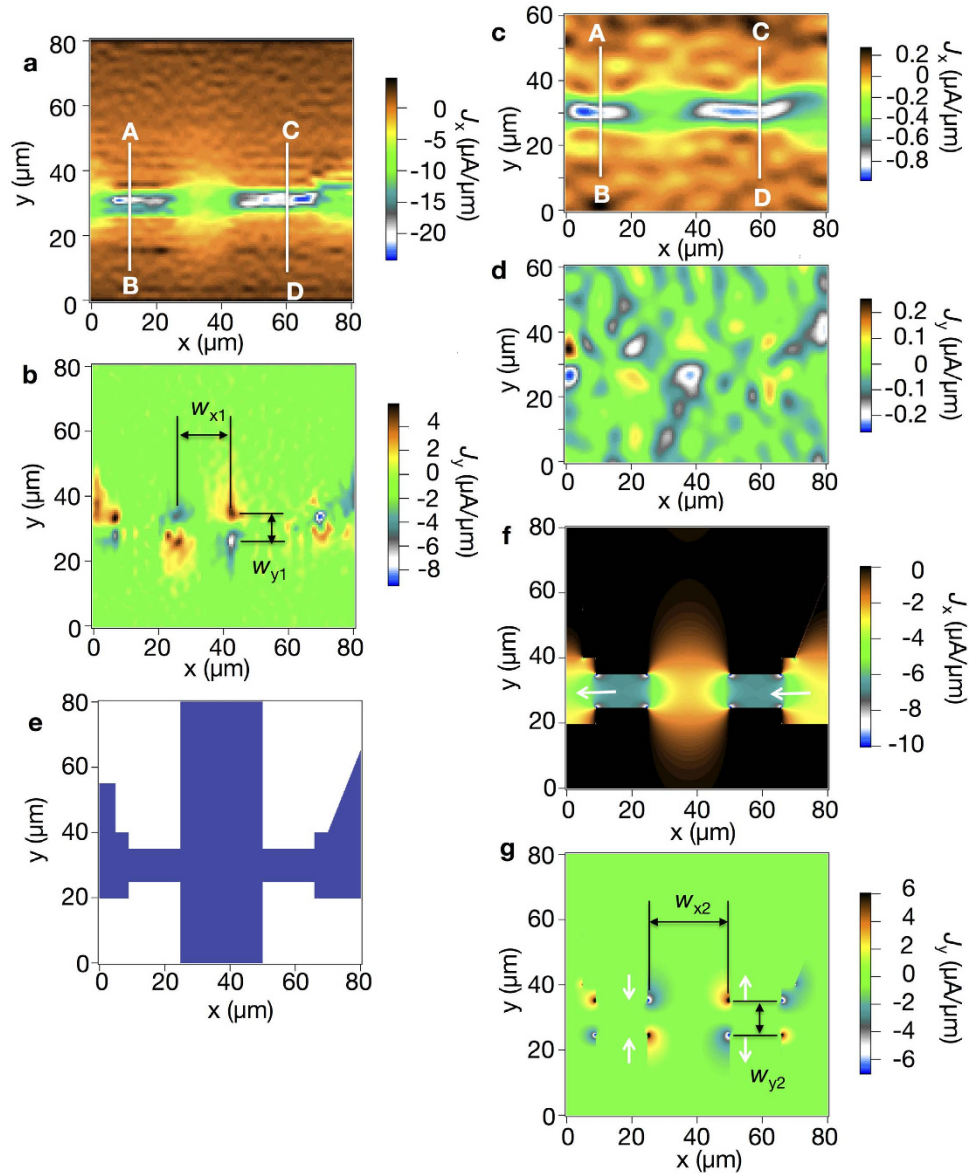


Figure 6. Reconstructed current density distributions and calculated current densities. (a) Reconstructed current density distributions $J_x(x, y)$ and (b) $J_y(x, y)$ from the measured magnetic flux in Fig. 5 at $I_{\text{sample}} = 70 \mu\text{A}$. (c) $J_x(x, y)$ and (d) $J_y(x, y)$ reconstructed from the measured magnetic flux in Fig. 5 at $I_{\text{sample}} = 2.8 \mu\text{A}$. (e) Pattern of Hall-bar structure assumed for $\sigma(x, y)$. Blue and white indicate area with $\sigma(x, y) = \sigma_0$ and $\sigma(x, y) = 0$, respectively. (f) Calculated current density $J_x(x, y)$ and (g) $J_y(x, y)$, assuming isotropic conductivity $\sigma(x, y)$. The white arrows indicate the direction of the current.

by a finite-difference method on a mesh of 400×400 with $\sigma_0 = 0.05 \text{ S}$, where $\phi(x, y)$ is the electrostatic potential. Conductivity was assumed to be $\sigma(x, y) = \sigma_0$ inside the Hall-bar structure and $\sigma(x, y) = 0$ elsewhere as shown in Fig. 6(e). Dirichlet boundary conditions were applied for x -direction, and the voltage was set to be -0.798 and 0 meV at $x = 0$ and $80 \mu\text{m}$, respectively. A periodic boundary condition was applied to the y -direction. The electrostatic potential $\phi(x, y)$ was converged to an accuracy of less than 10^{-6} V .

Figure 6(f,g) show calculated current density. The observed main features in Fig. 6(a,b) are reproduced in Fig. 6(f,g). In particular, the spread of $J_x(x, y)$ to the wider stem of the Hall-bar in Fig. 6(a) is reproduced in Fig. 6(f), and the local maxima and minima in $J_y(x, y)$ near the corners of the mesa structure of the Hall-bar in Fig. 6(b) are reproduced in Fig. 6(g). The distances between the local maxima and minima in $J_y(x, y)$ are $w_{x1} = 16 \mu\text{m}$ in Fig. 6(b) and $w_{x2} = 25 \mu\text{m}$ in Fig. 6(g), indicating a sizable disagreement with $w_{x1} < w_{x2}$, whereas the difference in w_{y1} in Fig. 6(b) and w_{y2} in Fig. 6(g) is small. This disagreement is not explained by the finite k_{max} for the truncation of high-frequency components

in the Fourier analysis. We calculated the magnetic field due to the calculated current density as given by equation (12), and reconstructed the current density distributions by changing k_{max} by the method described by equations (1)-(11) and checked that w_{x2} and w_{y2} did not depend on k_{max} . Consequently the disagreement between the observed and the calculated distances between the local maxima and minima in $J_y(x, y)$ is understood by the finite length that the electrons travel before they change momenta following the direction of the gradient of the electrostatic potential $\phi(x, y)$. The difference $w_{x2} - w_{x1} = 9 \mu\text{m}$ is reasonably explained by the mean free path of the sample of $8.7 \mu\text{m}$. Thus the disagreement between w_{x1} and w_{x2} is a manifestation of ballistic transport of the electrons. The reconstructed $J_x(x, y)$ in Fig. 6(a) is nearly symmetric and four main peaks in $20 < x < 50 \mu\text{m}$ in Fig. 6(b) are nearly antisymmetric with respect to the center of the $25 \mu\text{m}$ -width bar, because ac bias current was applied to the Hall-bar structure and the magnetic field was detected synchronously using a lock-in amplifier. The effect of the limited spatial resolution due to small k_{max} is observed in Fig. 6(a) where the current density is larger at the center of the Hall-bar than the edge unlike the case in Fig. 6(f) where the current density is nearly homogeneous across the stem of the Hall-bar with the width of $10 \mu\text{m}$. The depletion layer thickness was estimated to be $134 \text{nm}^{23,24}$ for similar GaAs single heterojunction sample with the electron density of $4.6 \times 10^{15} \text{m}^{-2}$. The height of the mesa structure of the sample was about 100nm . Thus the depletion layer thickness of the two-dimensional electron gas and the widths of the lateral etching are too small to explain the measured current density distribution. Improvements in the signal-to-noise ratio of the magnetic flux measurements are required to increase k_{max} to obtain better spatial resolution.

In summary, we have constructed a weak-link scanning nano-SQUID microscope using a SQUID probe with small hysteresis in I - V curve suitable for a magnetic sensor for scanning measurements. We have measured magnetic field distribution created by the current in the Hall-bar structure. Two-dimensional current density components $J_x(x, y)$ and $J_y(x, y)$ were reconstructed from measured B based on a Fourier analysis. The reconstructed two-dimensional current density reproduced most of the features of current density calculated by solving Laplace equation, however, a significant deviation was found near the corners of the Hall-bar structure and was explained by ballistic electron transport. Our newly developed scanning nano-SQUID microscope may contribute to characterize, for example, chiral or helical superconductors and current density in the quantum anomalous Hall effect or in the quantum spin Hall effect.

Methods

Low temperature scanning SQUID microscope. A nano-SQUID probe was accommodated in a rigid stainless housing connected with four springs to the 4 K plate of a cryogen-free pulse tube refrigerator (Optistat PT, Oxford Instruments) to reduce vibrations due to cooling cycle. A sample was mounted on closed loop inertially actuated triaxial stepping piezoelectric-stages with resistive position encoders (ANPx101/RES and ANPz101/RES, Attocube systems). The piezoelectric-stages were operated in the coarse positioning mode with typical minimum step size of 10nm and in the fine positioning mode. The repeatability of the resistive position encoders were estimated to be about 200nm at 4 K. The stainless housing was placed in the bore of a homemade superconducting magnet with the bore size of 50mm . Control of the distance between a nano-SQUID probe and the sample surface was made by monitoring the shift of the resonance frequency of a quartz tuning fork using a lock-in amplifier²⁵. First, the z -axis stage was moved by a step of about 100nm in the coarse positioning mode. Second, the z -axis stage was scanned by monitoring the signal of the quartz tuning fork in the fine positioning mode. This procedure was repeated until the resonance frequency shift of the quartz tuning fork due to the nano-SQUID probe-sample interaction was detected. After detecting the height of the sample surface, scanning of the nano-SQUID probe was performed at a constant height above the sample surface by monitoring the resistive position encoder. The voltage of a SQUID was amplified by a preamplifier (LI-75A, NF Corporation) at room temperature. The measurements were performed in unshielded laboratory environment. Because the size of the SQUID loop is small, the contribution from the environment magnetic field noise is relatively small. The noise of the SQUID probes is mainly limited by the equivalent input noise of the preamplifier.

Sample. The sample GaAs/ $\text{Al}_{0.3}\text{Ga}_{0.7}\text{As}$ modulation-doped single heterojunction consists of a GaAs/AlAs superlattice buffer layer, 200nm -thick undoped GaAs layer, 40nm -thick undoped $\text{Al}_{0.3}\text{Ga}_{0.7}\text{As}$ layer, 30nm -thick Si-doped $\text{Al}_{0.3}\text{Ga}_{0.7}\text{As}$ layer, and 10nm -thick Si-doped GaAs capping layer. The density and the mobility of the two-dimensional electron gas were $3.3 \times 10^{15} \text{m}^{-2}$ and $91 \text{m}^2/\text{Vs}$ at 2.8K , giving the mean free path of electrons of $8.7 \mu\text{m}$. A Hall-bar structure of the width and the length of 25 and $300 \mu\text{m}$ was fabricated by photolithography. The distance between the voltage probes was $100 \mu\text{m}$. Current between ohmic contacts of the Hall-bar structure was modulated at 1873Hz . The voltage of a SQUID probe at a constant current bias changes due to magnetic field created by the current in the Hall-bar structure. This voltage change was detected synchronously with a lock-in amplifier at a time constant of 1s by scanning the nano-SQUID probe on the surface of the sample.

References

1. Clarke, J. & Braginski, A. *The SQUID Handbook: Fundamentals and Technology of SQUIDs and SQUID Systems* (Wiley-VCH Verlag, 2004).
2. Hasselbach, K., Veauvy, C. & Mailly, D. Microsquad magnetometry and magnetic imaging. *Physica C* **332**, 140–147 (2000).
3. Gallop, J. SQUIDs: some limits to measurement. *Supercond. Sci. Technol.* **16**, 1575 (2003).
4. Faley, M. *et al.* High temperature superconductor dc SQUID micro-susceptometer for room temperature objects. *Supercond. Sci. Technol.* **17**, S324–S327 (2004).
5. Etaki, S. *et al.* Motion detection of a micromechanical resonator embedded in a d.c. SQUID. *Nat. Phys.* **4**, 785–788 (2008).
6. Vasyukov, D. *et al.* A scanning superconducting quantum interference device with single electron spin sensitivity. *Nat. Nano.* **9**, 639–644 (2013).
7. Ketchen, M. *et al.* Design, fabrication, and performance of integrated miniature SQUID susceptometers. *IEEE Trans. Magn.* **25**, 1212–1215 (1989).
8. Koshnick, N. C. *et al.* A terraced scanning superconducting quantum interference device susceptometer with submicron pickup loops. *Appl. Phys. Lett.* **93**, 243101 (2008).
9. Tokura, Y., Honda, T., Tsubaki, K. & Tarucha, S. Noninvasive determination of the ballistic-electron current distribution. *Phys. Rev. B* **54**, 1947–1952 (1996).
10. Matsumoto, T. *et al.* Fabrication of weak-link Nb-based nano-SQUIDs by FIB process. *Physica C* **471**, 1246–1248 (2011).
11. Cox, D. C., Gallop, J. C. & Hao, L. Focused ion beam processing of superconducting junctions and SQUID based devices. *Nanofabrication* **1**, 53–64 (2014).
12. Skocpol, W., Beasley, M. & Tinkham, M. Self-heating hotspots in superconducting thin-film microbridges. *J. Appl. Phys.* **45**, 4054–4066 (1974).
13. Hasselbach, K., Mailly, D. & Kirtley, J. R. Micro-superconducting quantum interference device characteristics. *J. of Appl. Phys.* **91**, 4432–4437 (2002).
14. Likharev, K. K. Superconducting weak links. *Rev. Mod. Phys.* **51**, 101–159 (1979).
15. Cage, M. E. *et al.* Dissipation and dynamic nonlinear behavior in the quantum Hall regime. *Phys. Rev. Lett.* **51**, 1374–1377 (1983).
16. Komiyama, S., Takamasu, T., Hiyamizu, S. & Sasa, S. Breakdown of the quantum Hall effect due to electron heating. *Solid State Commun.* **54**, 479–484 (1985).
17. Roth, B. J., Sepulveda, N. G. & Wikswo, J. P. Using a magnetometer to image a two-dimensional current distribution. *J. Appl. Phys.* **65**, 361–372 (1989).
18. Press, W. H., Teukolsky, S. A., Vetterling, W. T. & Flannery, B. P. *Numerical Recipes in C* (Cambridge University Press, Cambridge, 1988).
19. Reiser, M. Large-scale numerical simulation in semiconductor device modelling. *Comp. Meth. Appl. Mech. and Eng.* **1**, 17–38 (1972).
20. Fawcett, W., Boardman, A. & Swain, S. Monte carlo determination of electron transport properties in gallium arsenide. *J. Phys. Chem. Solids.* **31**, 1963–1990 (1970).
21. Hockney, R., Warriner, R. & Reiser, M. Two-dimensional particle models in semiconductor-device analysis. *Electron. Lett.* **10**, 484–486 (1974).
22. Laux, S. E., Kumar, A. & Fischetti, M. V. Analysis of quantum ballistic electron transport in ultrasmall silicon devices including space-charge and geometric effects. *J. Appl. Phys.* **95**, 5545–5582 (2004).
23. Ito, H. *et al.* Near-field optical mapping of quantum Hall edge states. *Phys. Rev. Lett.* **107**, 256803 (2011).
24. Mamyouda, S. *et al.* Circularly polarized near-field optical mapping of spin-resolved quantum Hall chiral edge states. *Nano Letters* **15**, 2417–2421 (2015).
25. Karrai, K. & Grober, R. D. Piezoelectric tip-sample distance control for near field optical microscopes. *Appl. Phys. Lett.* **66**, 1842–1844 (1995).

Acknowledgements

We would like to acknowledge Yuki Oshima for preparing Hall-bar samples. This work was partly supported by a Grant-in Aid for Scientific Research on Innovative Areas “Topological Quantum Phenomena” (Nos. 22103002, 25103704), “Topological Material Science” (No. 15H05853) from the Ministry of Education, Culture, Sports, Science and Technology (MEXT) of Japan and Grant-in-Aid for Scientific Research (Nos. 26610079, 15H03673) from Japan Society for the Promotion of Science. We thank Cryogenic Center at University of Tsukuba for technical assistance.

Author Contributions

S.N., S.K., R.I. and H.T. conceived the experiments, Y.S. and S.N. conducted the experiments, Y.S., H.K. and S.K. prepared SQUID probes, R.I. prepared a Au/Nb strip sample, Y.S. and S.N. analyzed the results. All authors reviewed the manuscript.

Additional Information

Supplementary information accompanies this paper at <http://www.nature.com/srep>

Competing financial interests: The authors declare no competing financial interests.

How to cite this article: Shibata, Y. *et al.* Imaging of current density distributions with a Nb weak-link scanning nano-SQUID microscope. *Sci. Rep.* **5**, 15097; doi: 10.1038/srep15097 (2015).



This work is licensed under a Creative Commons Attribution 4.0 International License. The images or other third party material in this article are included in the article’s Creative Commons license, unless indicated otherwise in the credit line; if the material is not included under the Creative Commons license, users will need to obtain permission from the license holder to reproduce the material. To view a copy of this license, visit <http://creativecommons.org/licenses/by/4.0/>